Precision measurement of hyperfine constants and isotope shift of the Rb $6S_{1/2}$ state via a two-photon transition

R. Ayachitula, M. D. Anderson, C. D. McLaughlin, and R. J. Knize
Department of Physics and Meteorology, Laser and Optics Research Center, United States Air Force Academy, 2354 Fairchild Drive, USAF Academy, Colorado 80840, USA

C. E. Mungan
Department of Physics, United States Naval Academy, Stop 9c, 572c Holloway Road, Annapolis, Maryland 21402, USA

M. D. Lindsay*
Lindsay Enterprises Inc. LLC, Estes Park, Colorado 80517, USA

(Received 20 December 2023; revised 28 May 2024; accepted 25 June 2024; published 5 August 2024)

Using Doppler-free two-photon spectroscopy of the Rb $5S_{1/2}$ to $6S_{1/2}$ transition in a temperature-controlled vapor cell, for both naturally occurring isotopes, we measure to high accuracy the hyperfine splittings and constants, as well as the isotope shift of the $6S_{1/2}$ state. We lock a tunable microwave-driven electro-optic modulator sideband of the 993-nm laser to an ultrastable high-finesse cavity, thus achieving microwave frequency accuracy for the relative laser tuning. The line shapes are fit with a Voigt profile to extract line centers in order to calculate the hyperfine splittings, magnetic dipole hyperfine constants, isotope shift, and hyperfine anomaly. For the hyperfine splittings of the $6S_{1/2}$ state in ^{85}Rb and ^{87}Rb, respectively, we find 717.195(3) MHz and 1614.709(3) MHz. For the hyperfine constants A for the $6S_{1/2}$ states, we find 239.065(2) MHz and 807.355(2) MHz for ^{85}Rb and ^{87}Rb, respectively, and −99.189(3) MHz for the isotope shift (^{85}Rb minus ^{87}Rb). These hyperfine splittings and constants are 10 to 25 times more accurate than previously published results. We measure the hyperfine anomaly $^{85}\Delta^{87}$ of the $6S_{1/2}$ state to be −0.00350(1), which is about 20 times more accurate than previously published results.

DOI: 10.1103/PhysRevA.110.022803

I. INTRODUCTION

Optical two-photon studies in Rb have produced measurements of absolute frequency from the ground state to multiple excited states [1–5], excited-state lifetimes [6,7], excited-state hyperfine splittings, and magnetic dipole hyperfine constants [8–15]. Such two-photon transitions in Rb are of interest for applications in providing stable frequency references for satellite navigation systems and for testing fundamental physics using precision measurements.

The atomic Rb frequency standard has been a preferred choice for timekeeping in space with its reduced size, weight, and power consumption (SWaP), and relatively low levels of frequency instability. Commercially available Rb microwave atomic clocks exhibit a fractional drift rate as low as a few parts in 10^{14} per day [16,17]. In principal, a clock based on narrow optical transitions operating at frequencies 10^5 times higher than microwave frequencies should be more stable. A compact optical clock based on a two-photon transition in a Rb vapor exhibiting a fractional drift rate of 4×10^{-15} per day was recently realized [18]. Higher stability clocks based on near-infrared two-photon transitions in thermal Rb vapor from the ground state to the $5D_{5/2}$ state or the $6S_{1/2}$ state could enhance the real-time capabilities of the global positioning system (GPS) in potential defense applications [19–21]. The $5S_{1/2}$ ground state and the $6S_{1/2}$ excited state both have the same Landé g factors and therefore the same magnetic field shifts. As a result, the $5S_{1/2} \rightarrow 6S_{1/2}$ transition is less susceptible to fluctuations due to stray magnetic fields, possibly making it superior to the $5S_{1/2} \rightarrow 5D_{5/2}$ transition for such applications.

The parity-forbidden dipole transition $5S_{1/2} \rightarrow 6S_{1/2}$ between the ground state and the first excited state of Rb has been proposed to study optical parity nonconservation [22]. Atomic parity violation studies of cesium have been performed as a low-energy precision means of testing the standard model [23–25]. The most precise measurement of the parity nonconserving $6S_{1/2} \rightarrow 7S_{1/2}$ transition amplitude was measured in ^{133}Cs [23,26].

In this work, we investigate the $5S_{1/2} \rightarrow 6S_{1/2}$ two-photon transition in a thermal Rb vapor at 993 nm. We measure the hyperfine splittings in the two naturally occurring isotopes, the hyperfine constants A for each isotope, and the isotope shift. The precision of our hyperfine constants allows us to determine an improved hyperfine anomaly value, which can lead to a better understanding of the Rb nuclear charge distribution and nuclear magnetization distribution [27,28], and thus the Rb nuclear wave function and structure, and how

*Current address: Department of Physics and Meteorology, Laser and Optics Research Center, United States Air Force Academy.

they change when two neutrons are added [29]. There has been some recent theoretical interest and work in calculating the Bohr-Weisskopf (BW) hyperfine anomaly in Cs and Rb, to test the atomic wave functions in the nuclear region at the 0.2% level [30], and to test the difference between the single-particle model and the uniform or Fermi models of nuclear magnetization [30].

II. THEORY

The one-photon electric dipole transition from ground state mS to excited state nS is forbidden. However, these excitations are accessible by two-photon processes and have selection rules $\Delta F = 0$ and $\Delta m_F = 0$ [31,32]. In 1931, Goppert-Mayer proposed two-photon processes in which two photons are simultaneously absorbed by an atom provided that the frequency sum of the two photons equals the excitation frequency of the atomic transition [33]. In 1970, Vasilenko *et al.* [34] noted that an atom in an electromagnetic standing wave of frequency ω would absorb two photons, i.e., a single photon from each beam, resulting in a first-order Doppler-free line shape. Assuming $\vec{v}$ is the atom velocity and $\vec{k}$ is the wave vector of light, the atom (in its rest frame) would absorb a photon of frequency $\omega + \vec{k}\cdot\vec{v}$ from one beam and a photon of frequency $\omega - \vec{k}\cdot\vec{v}$ from the other beam to go from the ground state E_g to the excited state E_e. The two-photon resonance condition in this case is [34]

$$E_e - E_g = \hbar(\omega + \vec{k}\cdot\vec{v}) + \hbar(\omega - \vec{k}\cdot\vec{v}) = 2\hbar\omega, \qquad (1)$$

showing that at resonance, all irradiated atoms, regardless of velocity, absorb one photon from each beam, resulting in a narrow first-order Doppler-free resonance.

These narrow-linewidth two-photon processes can be used to probe the interactions between a nuclear magnetic dipole and the magnetic field created by the electron at the nucleus. Furthermore, we can use the hyperfine interaction to study the magnetic moment distribution of the nucleus. The nuclear quadrupole interaction with the magnetic field gradient of the electrons vanishes for spherically symmetric $J = 0, \pm 1/2$ orbitals [35]. The hyperfine splitting of the S electronic states is due solely to the nuclear magnetic dipole moment interacting with the magnetic field of the electrons. The effect is strongest in S electronic orbitals because they have the largest overlap with the nucleus. For spherically symmetric S orbital states, the hyperfine constants B and C are exactly zero, and the hyperfine energy level shifts $E_{\rm hf}$ of the $6S_{1/2}$ hyperfine states are given by

$$E_{\rm hf} = \frac{A}{2}[F(F+1) - I(I+1) - J(J+1)], \qquad (2)$$

where A is the hyperfine magnetic dipole constant, F is the total angular momentum, I is the nuclear spin, and J is the electronic angular momentum. Moreover, under the approximation that the nuclear magnetic dipole moment of the atom is point sized, an expression for the hyperfine magnetic dipole constant is $A_{\rm hf,point} = \frac{4\mu_0}{3\pi\hbar} g_I \mu_I \mu_B |\psi(0)|^2 f_R$, where g_I is the nuclear g factor, μ_I is the nuclear magnetic dipole moment, μ_B is the Bohr magneton, $|\psi(0)|$ is the electronic wave function at the nucleus, and f_R takes into account relativistic effects [36]. The nuclear g factor is $g_I = \mu_I/I$. Because the nucleus has a finite size, it is not actually a point particle with a nuclear magnetic dipole moment. The hyperfine magnetic dipole constant is smaller than what would be expected for a point nucleus [37] and, as such, a more precise derivation of the constant involves adding two small corrections to the pointlike model $A_{\rm hf,extended} = A_{\rm hf,point}(1+\epsilon_{\rm BCRS})(1+\epsilon_{\rm BW})$. The first correction, i.e., the Breit-Crawford-Rosenthal-Schawlow correction ($\epsilon_{\rm BCRS}$), to the hyperfine interaction is due to modification of the electronic wave function by a uniform extended nuclear charge distribution. The second correction, i.e., the Bohr-Weisskopf correction ($\epsilon_{\rm BW}$), is determined by how the magnetization distribution throughout the nuclear volume affects the hyperfine interaction. The electronic wave function of different alkali isotopes in the nucleus to a good approximation is the same, so the ratio of the pointlike hyperfine constants of two different Rb isotopes is roughly $A_{85}/A_{87} = g_{I_{85}}/g_{I_{87}}$.

However, precision experiments can measure anomalies from this pointlike description of the hyperfine constants of the different isotopes. Deviations from this pointlike description can be modeled by [27]

$$\frac{A_{85}}{g_{I_{85}}}\frac{g_{I_{87}}}{A_{87}} = 1 + {}^{85}\Delta^{87}, \qquad (3)$$

where the differential hyperfine anomaly is ${}^{85}\Delta^{87} = (\epsilon^{85}_{\rm BCRS} - \epsilon^{87}_{\rm BCRS}) + (\epsilon^{85}_{\rm BW} - \epsilon^{87}_{\rm BW})$. Because there is less than 1% difference in the mean nuclear charge radii of the two Rb isotopes, the BCRS correction between the two isotopes, $(\epsilon^{85}_{\rm BCRS} - \epsilon^{87}_{\rm BCRS})$ can be neglected [29,38], making the Bohr-Weisskopf correction dominant in the hyperfine anomaly [27].

The differential effect of the finite size of the nucleus and the difference in the mass of the two isotopes results in a measurable isotope shift in the electronic energy levels of ^{85}Rb and ^{87}Rb.

III. EXPERIMENT

Rubidium atoms in a thermal vapor are excited from the $5S_{1/2}$ ground state to the $6S_{1/2}$ excited state through a virtual state by absorbing two 993-nm photons as shown in Fig. 1. Atoms decay back to the ground state through the D1 transition or the D2 transition. An atom decaying through the D1 line emits a 1324 -nm photon to reach $5P_{1/2}$, and then emits a 795 -nm photon to decay back to the ground state. An atom decaying to the ground state through the D2 line first emits a 1367 -nm photon to reach the $5P_{3/2}$ level, followed by a 780 -nm photon to decay to the ground state. We detect 780 -nm fluorescence photons using a filtered photomultiplier tube (PMT).

To excite the two-photon transition, we use a Toptica model DLC-TA-SHG Pro single-frequency continuous-wave tapered amplifier diode laser system, with a maximum output power of 850 mW at 993 nm and a single-mode tuning range of approximately 15 GHz. A block diagram of the experiment is shown in Fig. 2. A semiconductor tapered optical amplifier increases the power of the 993-nm laser before it is directed into the experiment. The main linearly polarized laser beam is split into two beams at a 50/50 nonpolarizing beam splitter. After the beam splitter, the equally intense collinear counterpropagating beams pass through a quartz Rb vapor cell.

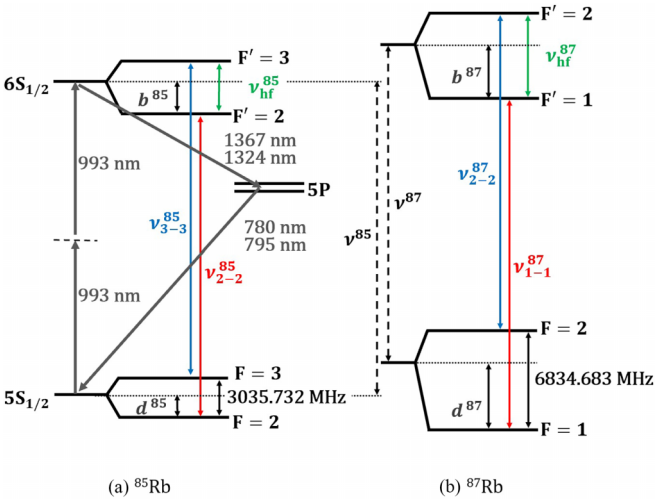

(a) ^{85}Rb (b) ^{87}Rb

FIG. 1. Energy diagrams for (a)^{85}Rb and (b)^{87}Rb (not drawn to scale). The ground-state $5S_{1/2}$ hyperfine splittings are more than a factor of four larger than the $6S_{1/2}$ hyperfine splittings. The transition frequencies corresponding to the four actual observed transitions are shown as ν^{85}_{2-2}, ν^{85}_{3-3}, ν^{87}_{1-1}, and ν^{87}_{2-2}. These four transitions are used to calculate the $6S_{1/2}$ hyperfine splittings, $\nu^{85}_{\rm hf}$ and $\nu^{87}_{\rm hf}$. The $5S_{1/2} \rightarrow 6S_{1/2}$ centroid frequency differences for each isotope are also shown as ν^{85} and ν^{87}. These centroid frequencies are used to calculate the isotope shift $\nu^{85} - \nu^{87}$.

The beams are not focused and both have a FWHM diameter of about 2.5 mm in the cell. Laser-induced fluorescence at 780 nm is detected by a PMT equipped with a short-pass filter stack and a 780 -nm narrow line filter to eliminate detection of 993-nm light. In order to measure the hyperfine splittings and isotope shift to a high accuracy, a small pick-off beam is sent to a 10 -GHz bandwidth electro-optic modulator (EOM). A WindFreak SynthPro microwave synthesizer modulates this EOM in the range between 800 and 3500 MHz to create optical sidebands. The lower sideband is locked to one fringe of an ultrastable cavity with a finesse of 300 000 and a free spectral range of 1.5 GHz, locking the laser optical frequency at an offset microwave frequency relative to the ultrastable

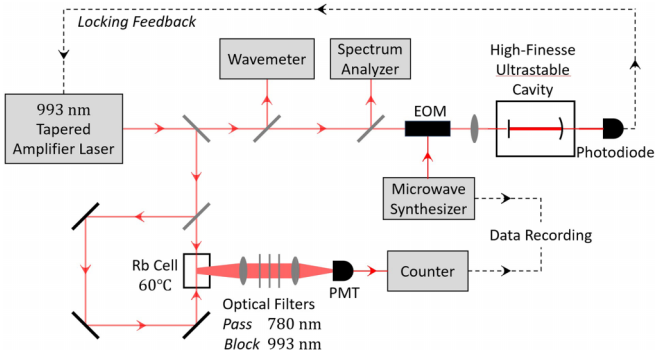

FIG. 2. Experiment block diagram. The 993-nm laser is passed to a wave meter, a spectrum analyzer, and a high-bandwidth EOM driven by a microwave synthesizer. The lower sideband of the EOM is locked to an ultrastable cavity. The frequency is scanned over the four Rb transitions shown in Fig. 1 by tuning the microwave synthesizer.

optical cavity. The lower sideband is locked to this same fringe throughout the experiment. The laser is scanned over the $5S_{1/2}$ to $6S_{1/2}$ transitions for each isotope by tuning the microwave synthesizer. We record the microwave frequency difference between the lower sideband and the transition frequency of the main 993-nm beam. We know this difference to kilohertz accuracy from the microwave synthesizer. Therefore, the relative tuning of the main laser beam is also known to the same high degree of accuracy. The ultrastable cavity drift is measured to be 13 kHz/day, but within the time required for the scans of the two hyperfine lines of one isotope (about 50 minutes), the drift is no more than 0.5 kHz. In order to tune the laser to the four separate transitions, two additional pick-off beams are taken from the main beam: one is sent to a spectrum analyzer to examine and verify the spectral mode of the laser and the other is sent to a Bristol 621A wave meter, with an absolute accuracy of 30 MHz, to roughly determine the laser wavelength's proximity to the transition wavelength.

The fused-quartz Rb cell is placed inside an anodized aluminum housing, and compressed air is heated and flowed across the cell. The housing is wrapped in aluminum foil to stabilize the temperature of the cell. On the basis of the cell temperature, we calculate the Rb density. Using a graph of the vapor pressure versus temperature [39,40], we convert the cell temperature T to the vapor pressure of Rb P. Using the ideal gas law, $n = P/kT$ at 60 °C, the atomic density of Rb is calculated to be $n = 3.0 \times 10^{11}$ atoms/cm^3. The experiments are performed at 60 °C in the low-temperature regime, where we are able to minimize the pressure broadening while retaining a good signal-to-noise ratio.

Helmholtz coils are used to minimize ambient magnetic fields. We measure the residual field to be less than 0.5 μT in all three dimensions in the 2 cm^3 interaction region. We find that turning off and turning on the B-field reduction coils has no effect on the line centers, to within 3 kHz.

A PMT (Hamamatsu R636) is used to detect the 780 -nm cascade fluorescence from the $6S_{1/2}$ state decaying to the $5S_{1/2}$ ground state through the $5P_{3/2}$ state. We implement a few techniques to reduce the detection of scattered 993-nm light to improve the signal-to-noise ratio. A short-pass filter with a cutoff wavelength of 850 nm is also placed between the cell and the PMT. In addition, the PMT has a quantum efficiency 100 times lower at 993 nm than at 780 nm. In an effort to further limit the detection of the 993-nm photons, we use a narrow-bandpass filter centered at 780 nm. Due to this, we inadvertently filter out the 795 -nm light of the D1 line.

To measure the hyperfine splittings, we scan the laser across the peak of each transition by controlling the microwave frequency driving the EOM sideband. The resulting line shape is a narrow Doppler-free peak on top of a broad but shallow Doppler pedestal. The line shape for atoms interacting with two counterpropagating beams is nominally a Doppler-free Lorentzian profile. The atoms can also absorb two copropagating photons from one beam such that the Doppler shifts do not cancel. In this case, the atoms absorb given that the energy defect $E_e - E_g - 2\hbar\omega$ is equal to the Doppler shift $\pm 2kv\cos\theta$. When the polarization of the beams is the same, the probability of absorbing one photon from each counterpropagating beam is four times the probability of absorbing two photons from the same beam [41].

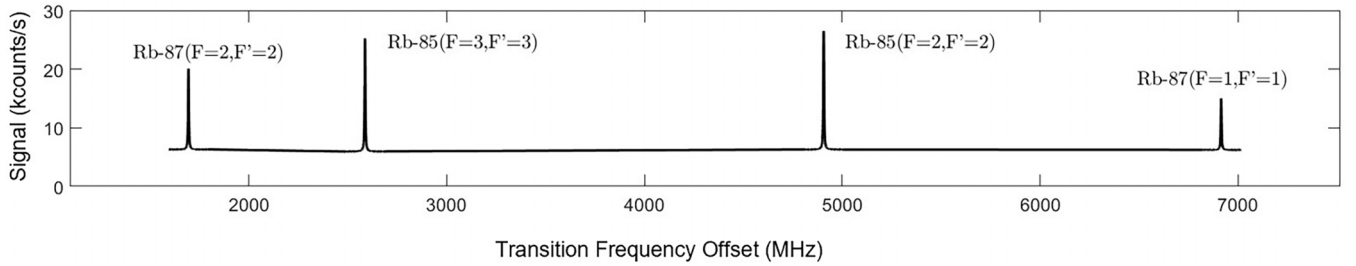

FIG. 3. The four observed spectra of the $5S_{1/2} \rightarrow 6S_{1/2}$ transition showing signal in kcounts/s vs transition frequency offset in MHz.

If the excitation beams are not exactly antiparallel or if the beam is diverging as it passes through the cell, there is a component of $\vec{k}$ that is perpendicular to the beam axis, resulting in a slight Doppler broadening of the central peak. To minimize the broadening caused by beam divergence, we leave the beams unfocused. To limit the broadening from exciting the atoms with beams that are not perfectly antiparallel, we aligned the beams by observing the interference pattern created by the two counterpropagating beams recombining at the beam splitter after passing through the Rb cell. These mechanisms add slight symmetric Doppler broadening to our central peak, but do not cause a systematic shift of the line center to within 3 kHz. The absorption of our Doppler-broadened two-level system as a function of laser frequency is nevertheless well modeled by a Voigt profile. Voigt fits of the absorption line shapes are performed on each of the four Rb transitions to extract the line centers and the Gaussian and Lorentzian FWHM widths. The line centers and widths are microwave frequencies that correspond to the absorption of two photons to make the transition.

Additional broadening mechanisms, such as power broadening and pressure broadening, are suppressed by performing experiments at one-fifth the maximum laser power (160 mW) and a low cell temperature (60 °C). These mechanisms result in symmetric broadening of the line about the center frequency and do not change the line center itself to within our statistical uncertainty. The second-order Doppler effect is negligible to within 100 Hz.

IV. RESULTS AND DISCUSSION

A. Two-photon spectra

We measure the count rate of 780-nm fluorescence photons using a PMT. Operating our laser at 160 mW, we have a signal-to-noise ratio of $77\sqrt{\tau}$, where τ is the integration time, which is 1 s for these data. The background rate due to nonresonant scattered light and PMT dark counts is 6000 counts/s, whereas our two-photon signal peaks at 12 000 counts/s. In one 500-point scan, we ramp the frequency from 50 MHz below the approximate nominal central frequency of the transition to 50 MHz above it. We record roughly 10 times more data points in the central 30 MHz of the scan to obtain finer resolution in the center of the spectrum, as well as in the upward and downward slopes of the spectrum peak. We ramp the microwave frequency upward and measure the spectrum and subsequently scan the frequency downward and measure the spectrum. We find no difference between the line centers of the upward scan and the downward scan to within 2 kHz. Upon adding and removing a reference beam to normalize any laser output power fluctuations, we observe consistent power levels during a scan with no notable shift in the line position, regardless of whether or not we normalize the scan signal with this reference beam.

The two-photon transition selection rules allow for transitions only between levels of the same hyperfine quantum number ($\Delta F = 0$) [31,32], so we only observe the following four transitions (shown in Fig. 3): ^{85}Rb($F = 2 \rightarrow F' = 2$), ^{85}Rb($F = 3 \rightarrow F' = 3$), ^{87}Rb($F = 1 \rightarrow F' = 1$), and ^{87}Rb($F = 2 \rightarrow F' = 2$). A typical spectrum of the ^{87}Rb($F = 1 \rightarrow F' = 1$) transition is shown in Fig. 4. The two-photon transition microwave frequency offset shown on the horizontal axis is measured with respect to the fixed ultrastable cavity resonance fringe. The horizontal axis shows the change in the frequency sum of the two absorbed microwave photons, one for each of the two absorbed laser photons.

We fit our spectra using the nonlinear Voigt fitting function of the software program ORIGIN. The fitting program uses a Levenberg-Marquart algorithm to minimize residuals based on the shot noise. The Voigt line centers and their uncertainties are determined with reduced χ-squared values that

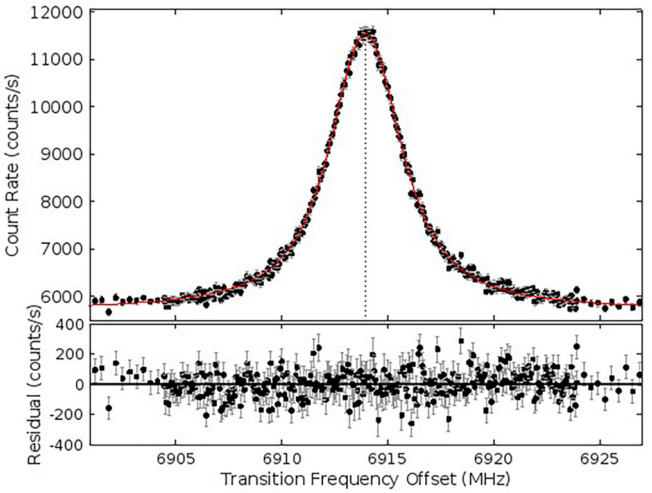

FIG. 4. A typical data set. The top figure is a plot of the ^{87}Rb($F = 1 \rightarrow F' = 1$) transition rate in counts per second vs the two-photon microwave frequency offset in MHz. The Voigt fit to the data is shown as a solid red line. The bottom figure shows the residuals of the Voigt fit as a function of microwave frequency offset. These residuals are of the order of the shot noise.

TABLE I. Comparison of hyperfine splittings and magnetic dipole hyperfine constants of the $6S_{1/2}$ state in ^{85}Rb and ^{87}Rb.

	^{85}Rb(MHz)		^{87}Rb(MHz)	
$\nu_{\rm hf}$	717.195(3)[a]	(this work)	1614.709(3)[a]	(this work)
	717.54(10)[a]	[46]	1615.32(16)[a]	[46]
A	239.065(2)[a]	(this work)	807.355(2)[a]	(this work)
	239.18(3)[a]	[46]	807.66(8)[a]	[46]
	239.3(1.2)[a]	[47]		
	238.2[b]	[48]		

[a]Experimental.
[b]Theoretical.

range from 1.10 to 2.05. Lorentzian fits are also performed, but they result in larger reduced χ-squared values. A small systematic shift of 0.5 kHz to 2.0 kHz is measured between the set microwave frequency and the actual frequency output from the synthesizer, and the Voigt line centers for each data run are corrected by twice this shift to incorporate the energy change due to the absorption of two photons. Larger microwave frequencies require larger corrections. For the sample data set shown in Fig. 4, a Voigt fit gives a two-photon transition line center of 6913.950(7) MHz, a Lorentzian width (FWHM) of 3.514(58) MHz, and a Gaussian width (FWHM) of 1.468(98) MHz. The reduced χ-squared value is 1.18. The Lorentzian spectral width (FWHM) of the $6S_{1/2}$ state corresponds to a lifetime of 45.29(75) ns. This lifetime is consistent with the 45.57(17) ns lifetime measurement of Gomez *et al.* [6] and the 45(5) ns lifetime measurement of Marek *et al.* [42].

In fitting our spectra, we consider the line-center shift due to one hyperfine line's roughly 500 MHz Gaussian Doppler width on another hyperfine line about 900 MHz or more away. Since the counterpropagating two-photon Voigt line strength is an order of magnitude larger and two orders of magnitude narrower than the copropagating Gaussian peak, the line-center pulling shift is no more than 0.3 kHz in the worst case of the two closest peaks, ^{87}Rb($F = 2 \rightarrow F' = 2$) and ^{85}Rb($F = 3 \rightarrow F' = 3$). In the worst case, we estimate that the error in the hyperfine splittings would be double the shift of one single line. We include this shift in our error budget in Table II. We also fit our lines using flat, tilted, and curving backgrounds and find no significant change in the center of the fitted line to within 3 kHz.

In Table II, we also consider the effect of the AC Stark shift and the Rb-Rb pressure shift on the spectral lines. The AC Stark shift for any one of the four allowed transitions is calculated to be −0.2 kHz and the Rb-Rb pressure shift is measured by Zameroski *et al.* [43] to be 2 kHz, but these differential shifts for the hyperfine splittings (one line center frequency subtracted from another) will be about 10^6 times smaller and therefore negligible. The uncertainties resulting from both are determined to be insignificant with respect to our statistical error.

We consider the possibility of a quantum interference line shift due to the fluorescence photon collection geometry and interference in the decay pathways from the upper excited states [44,45]. However, due to our strict selection rule ($\Delta F = 0$) [31,32], we have only one possible excited state from a given lower state, so there is no quantum interference and no line shift due to this mechanism.

TABLE II. Error budget (in kHz) for hyperfine splittings measurement in ^{87}Rb. The correction value in the hyperfine splitting and the uncertainty in that value are shown. The correction to a single line-center frequency is, in some cases, larger than the correction we show for the splitting, which involves the subtraction of two line-center frequencies.

Correction source	Value	Error
Ultrastable cavity drift	0.3	0.3
Pulse pile-up	0	0
Power broadening	0	0
Differential AC Stark shift	0	0
Differential pressure shift	0	0
Differential second-order Doppler shift	0	0
Line-pulling shift	−0.6	0.1
Microwave frequency reference	1.5	0.4
Statistical error[a]	0	2.0

[a]Standard error of the mean.

B. Hyperfine splittings

Several ^{85}Rb and ^{87}Rb spectra are collected to determine the hyperfine splittings, $\nu_{\rm hf}^{85}$ and $\nu_{\rm hf}^{87}$, shown in Fig. 1. Voigt fits are performed on the ^{85}Rb($F = 3 \rightarrow F' = 3$) and the ^{85}Rb($F = 2 \rightarrow F' = 2$) spectra individually. From the Voigt fits, we extract the transition line-center frequencies measured with respect to the $5S_{1/2}$ ground state. Doubling these frequencies gives us the frequencies of the two-photon transitions, shown as ν_{3-3}^{85} and ν_{2-2}^{85} in Fig. 1. We then calculate the hyperfine splitting for the $6S_{1/2}$ state of the ^{85}Rb isotope, $\nu_{\rm hf}^{85}$, by taking the frequency difference between the ground-state hyperfine splitting and the energy difference of the two individual two-photon transitions. For ^{85}Rb, the $6S_{1/2}$ hyperfine splitting is found using $\nu_{\rm hf}^{85} = 3035.732\,\text{MHz} - (\nu_{2-2}^{85} - \nu_{3-3}^{85})$, where 3035.732 MHz is the ground-state hyperfine splitting of the $5S_{1/2}$ state of ^{85}Rb [39]. The $6S_{1/2}$ hyperfine splitting for ^{87}Rb is found by calculating $\nu_{\rm hf}^{87} = 6834.683\,\text{MHz} - (\nu_{1-1}^{87} - \nu_{2-2}^{87})$, where 6834.683 MHz is the $5S_{1/2}$ ground-state hyperfine splitting for ^{87}Rb [40].

Averaging the hyperfine splittings determined for each individual transition pair gives $\nu_{\rm hf}^{85} = 717.195(3)$ MHz and $\nu_{\rm hf}^{87} = 1614.709(3)$ MHz, as shown in Table I and by the dashed blue lines in Fig. 5. The total uncertainty in the hyperfine splitting of ^{87}Rb is determined using the error budget listed in Table II. All errors are reported in kilohertz and are associated with the two-photon process. The statistical error for each isotope is reported as the standard error of the mean for its data set. The error budget for the hyperfine splitting in ^{85}Rb is very similar to that of Table II, resulting in the same total uncertainty. The standard deviation of each data set is shown in Fig. 5. From the $6S_{1/2}$ hyperfine splittings, the hyperfine constants A are determined using Eq. (2) and are listed in Table I. The hyperfine constants resulting from these average hyperfine splittings, calculated to be 239.065(2) MHz and 807.355(2) MHz, are listed in Table I along with values from previous experimental and theoretical work.

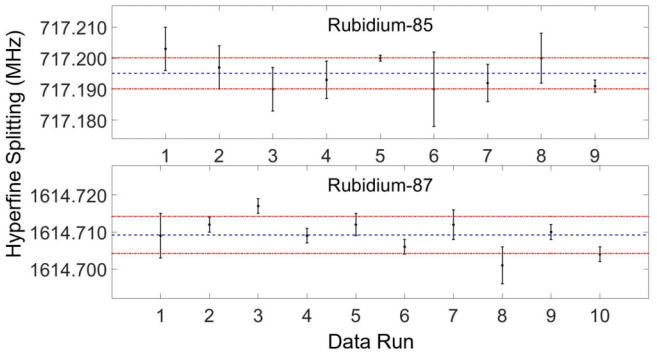

FIG. 5. The hyperfine splitting for each data run. The dashed blue line marks the average hyperfine splitting value and the red lines above and below the dashed blue line show the standard deviation of the measurement.

C. Isotope shift

The isotope shift (IS) of the $5S_{1/2} \rightarrow 6S_{1/2}$ transition is determined by the splitting of the ^{85}Rb and ^{87}Rb hyperfine lines. In principle, it is calculated by subtracting the two centroid transition frequencies marked ν^{85} and ν^{87} in Fig. 1. These centroid transitions are not real transitions, but are determined by setting the hyperfine interaction to zero. They contain large optical transition frequencies that are not measured accurately. In contrast, the relative (not absolute) frequency of each hyperfine transition that we measure in this paper is very accurately known as a microwave frequency offset from one single ultrastable cavity fringe. Therefore, the difference in the microwave frequency offsets for the ^{85}Rb and ^{87}Rb lines allows the large optical frequency offset of both lines to be subtracted exactly. In order to calculate the IS, all that is left is to take into account the well-known splitting of the $5S_{1/2}$ ground state, and our measured microwave frequency offsets (from the ultrastable cavity fringe, which is the same for both isotopes) of the ^{85}Rb and ^{87}Rb hyperfine lines.

With reference to Fig. 1, we calculate

$$\mathrm{IS} = \nu^{85} - \nu^{87} = \left(\nu^{85}_{2-2} + b^{85} - d^{85}\right) - \left(\nu^{87}_{1-1} + b^{87} - d^{87}\right), \tag{4}$$

where d^{85} and d^{87} are the frequency shifts from the $5S_{1/2}$ centroid to the lowest $5S_{1/2}$ hyperfine state ($F = 2$ for ^{85}Rb and $F = 1$ for ^{87}Rb), which are 1770.8439 MHz and 4271.6766 MHz, respectively [39,40]. In Eq. (4), b^{85} and b^{87} are the frequency shifts from the $6S_{1/2}$ centroid to the lowest $6S_{1/2}$ hyperfine state ($F = 2$ for ^{85}Rb and $F = 1$ for ^{87}Rb), which are 418.3638 MHz and 1009.1931 MHz, respectively. These b values are calculated to be 7/12 and 5/8 of the $6S_{1/2}$ hyperfine splittings shown in Table I. Thus, Eq. (4) simplifies to

$$\mathrm{IS} = \left(\nu^{85}_{2-2} - \nu^{87}_{1-1}\right) + 1910.003\,\mathrm{MHz}. \tag{5}$$

Each of ν^{85}_{2-2} and ν^{87}_{1-1} contains the large optical transition frequency, but the difference $\nu^{85}_{2-2} - \nu^{87}_{1-1}$ subtracts it out and is simply the difference in the (doubled) microwave frequency offset from the (same) ultrastable cavity reference fringe of the 85 and 87 lines (the ^{85}Rb to ^{87}Rb line splitting), which is measured to high accuracy.

TABLE III. Our A constants and g_I values from previous work [49,50] used to calculate the hyperfine anomaly of the $6S_{1/2}$ state using ^{85}Rb and ^{87}Rb. The hyperfine anomaly values shown as data points (a) and (b) in Fig. 6 are calculated using our A constants and the g_I values from [49,50], as shown below. The preferred value is $-0.00350(1)$. The other anomaly value labeled (b) is shown only to compare with the value of Ref. [46], which used the newer but less accurate g_I values of Ref. [50].

A_{85}		239.065(2) MHz (this work)	
A_{87}		807.355(2) MHz (this work)	
Label on Fig. 6		$g_I \times 10^5$	Hyperfine anomaly
(a)	$g_{I_{85}}$	0.2936400(6) [49]	$-0.00350(1)$
	$g_{I_{87}}$	0.9951414(10) [49]	
(b)	$g_{I_{85}}$	0.293636(22) [50]	$-0.00354(8)$
	$g_{I_{87}}$	0.995170(44) [50]	

Our average value for the inter-isotope splitting $\nu^{85}_{2-2} - \nu^{87}_{1-1}$ is -2009.192 MHz, so we find that the isotope shift is $-99.189(3)$ MHz. Our value is consistent with the only other previous $6S_{1/2}$ state isotope shift measurement of $-94(12)$ MHz by Orson *et al.* [4].

D. Hyperfine anomaly

The precision of our hyperfine magnetic dipole constants allows us to calculate the values for the hyperfine anomaly ($^{85}\Delta^{87}$ or HFA), as reported in Table III and shown in Fig. 6. Using our measured hyperfine constants and the accurate values of g_I of White *et al.* [49], we calculate the HFA for $6S_{1/2}$ as $-0.00350(1)$. Shown as data point (a) in Fig. 6, this is our preferred value. Using the newer but less accurate g_I values of Duong *et al.* [50], we obtain an HFA value of $-0.00354(8)$, shown as the data point (b) in Fig. 6.

In previous work, Perez Galvan *et al.* [46], using g_I values from Duong *et al.* [50], found the HFA to be $-0.0036(2)$, shown as the data point (c) in Fig. 6.

The HFA value for $5S_{1/2}$ is shown as point (d) in Fig. 6 [51]. Morzynski *et al.* [3] and Barmes *et al.* [52] measured precise values of hyperfine constants for the $7S_{1/2}$ state using two-photon spectroscopy with an optical frequency comb reference, but did not report values for the HFA. Using g_I values from White *et al.* [49], the HFA values of Morzynski and

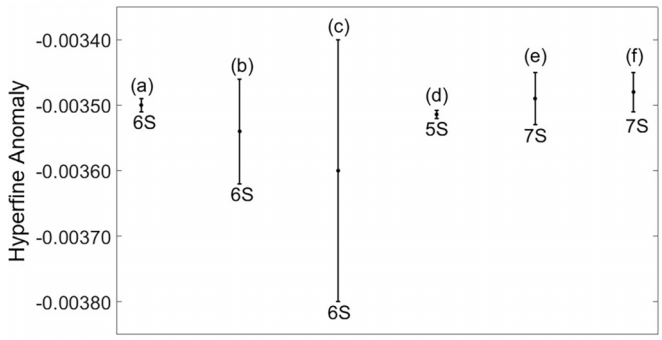

FIG. 6. Hyperfine anomaly values of various S states of Rb. The results obtained in this work correspond to data points (a) and (b).

Barmes are calculated to be −0.00348(3) and −0.00349(4), respectively, and are shown as data points (e) and (f) in Fig. 6. The HFA values are seen to be independent of the principal quantum number n, as predicted by Bohr and Weisskopf [37].

V. CONCLUSIONS

We calculate the hyperfine splitting of the $6S_{1/2}$ state in ^{85}Rb and ^{87}Rb by measuring the Doppler-free two-photon spectra of the four hyperfine lines allowed by the two-photon selection rules. These hyperfine splittings allow us to calculate hyperfine constants that are 25 times more accurate than the previous measurements [46]. Our values of the hyperfine constants and splittings, listed in Table I, are smaller than the values of Perez Galvan *et al.* [46] by approximately 3.5 standard deviations, and our values have errors that are a factor of at least 10 smaller. We attribute this difference to the complex two-color laser excitation and line-center determination scheme of Ref. [46]. Their two-color laser scheme leads to substantial Doppler broadening of the lines, in contrast to our one-color laser scheme. We also determine an isotope shift that is 4000 times more accurate than the previous measurement [4].

The small uncertainty in our measured hyperfine constants for both isotopes allows us to accurately determine the hyperfine anomaly. The uncertainty in our hyperfine anomaly value is dominated by the uncertainty in the g_I values, so we perform calculations with two sets [49,50] of nuclear values. The hyperfine anomaly values that we obtain are consistent with, but 20 times more accurate than, the previous best experimental measurements [46].

Precision measurements of atomic hyperfine structure and anomalies are critical to accurate modeling of electronic wave functions across the nucleus, where the weak interaction is mediated by Z-boson exchange between the electrons and the nucleus [53].

Atomic parity violation of the weak interaction is dependent on the choice of model describing the nuclear magnetization. The experimentally determined differential hyperfine anomaly in Cs has supported the use of the single-particle model of nuclear magnetization instead of the uniform magnetization model [30]. The improved value of the Rb differential hyperfine anomaly measured in this work, primarily due to the ϵ_{BW} correction of the anomaly, can help guide and verify new calculations of the nuclear magnetization moment distribution inside the nucleus. Recent calculations of this kind have been performed for Cs [30], and similar calculations could be done for Rb, which would enable a test of atomic wave functions in the nuclear region at the 0.2% level [30], and would help in the development of precision atomic many-body methods [30]. Precise calculations of wave functions for alkali atoms are needed for tests of parity nonconservation in atomic systems [54].

All data that support the findings of this study are included within the article or are available from the authors.

ACKNOWLEDGMENTS

This material is based on research sponsored in part by Lindsay Enterprises Inc., LLC under Agreement No. FA7000-21-2-0010. The U.S. Government is authorized to reproduce and distribute reprints for governmental purposes notwithstanding any copyright notation thereon. The views and conclusions contained herein are those of the authors and should not be interpreted as necessarily representing the official policies or endorsements, either expressed or implied, of the U.S. Air Force Academy or the U.S. Government. This work is approved for public release: the distribution is unlimited.

[1] H.-C. Chui, M.-S. Ko, Y.-W. Liu, J.-T. Shy, J.-L. Peng, and H. Ahn, Opt. Lett. **30**, 842 (2005).
[2] C. Glaser, F. Karlewski, J. Kluge, J. Grimmel, M. Kaiser, A. Günther, H. Hattermann, M. Krutzik, and J. Fortágh, Phys. Rev. A **102**, 012804 (2020).
[3] P. Morzyński, P. Wcisło, P. Ablewski, R. Gartman, W. Gawlik, P. Masłowski, B. Nagórny, F. Ozimek, C. Radzewicz, M. Witkowski, R. Ciuryło, and M. Zawada, Opt. Lett. **38**, 4581 (2013).
[4] S. T. Orson, C. D. McLaughlin, M. D. Lindsay, and R. J. Knize, J. Phys. B **54**, 175001 (2021).
[5] T. Nieddu, T. Ray, K. S. Rajasree, and S. Nic Chormaic, Opt. Express **27**, 6528 (2019).
[6] E. Gomez, F. Baumer, A. D. Lange, G. D. Sprouse, and L. A. Orozco, Phys. Rev. A **72**, 012502 (2005).
[7] M. S. Safronova, C. J. Williams, and C. W. Clark, Phys. Rev. A **69**, 022509 (2004).
[8] B. P. Stoicheff and E. Weinberger, Can. J. Phys. **57**, 2143 (1979).
[9] F. Nez, F. Biraben, R. Felder, and Y. Millerioux, Opt. Commun. **102**, 432 (1993).
[10] T. T. Grove, V. Sanchez-Villicana, B. C. Duncan, S. Maleki, and P. L. Gould, Phys. Scr. **52**, 271 (1995).
[11] M. J. Snadden, A. S. Bell, E. Riis, and A. I. Ferguson, Opt. Commun. **125**, 70 (1996).
[12] P. Otto, M. Gamperling, M. Hofacker, T. Meyer, V. Pagliari, A. Stifter, M. Krauss, and W. Hüttner, Chem. Phys. **282**, 289 (2002).
[13] P. Morzynski, P. Wcisło, P. Ablewski, R. Gartman, W. Gawlik, P. Masłowski, B. Nagórny, F. Ozimek, C. Radzewicz, M. Witkowski, R. Ciuryło, and M. Zawada, J. Phys.: Conf. Ser. **548**, 012023 (2014).
[14] J. Morgenweg, I. Barmes, and K. S. E. Eikema, Nat. Phys. **10**, 30 (2014).
[15] M. Allegrini, E. Arimondo, and L. A. Orozco, J. Phys. Chem. Ref. Data **51**, 043102 (2022).
[16] B. Jaduszliwer and J. Camparo, GPS Solut. **25**, 27 (2021).
[17] F. Vannicola, R. Beard, J. White, K. Senior, M. Largay, and J. Buisson, in *Proceedings of the 42nd Annual Precise Time and*

Time Interval Systems and Applications Meeting (Institute of Navigation, 2010), pp. 181–196.
[18] N. Lemke, K. W. Martin, R. Beard, B. K. Stuhl, A. J. Metcalf, and J. D. Elgin, Sensors **22**, 1982 (2022).
[19] K. W. Martin, G. Phelps, N. D. Lemke, M. S. Bigelow, B. Stuhl, M. Wojcik, M. Holt, I. Coddington, M. W. Bishop, and J. H. Burke, Phys. Rev. Appl. **9**, 014019 (2018).
[20] V. Formichella, J. Camparo, I. Sesia, G. Signorile, L. Galleani, M. Huang, and P. Tavella, J. Appl. Phys. **120**, 194501 (2016).
[21] L. Maleki and J. Prestage, Metrologia **42**, S145 (2005).
[22] V. A. Dzuba, V. V. Flambaum, and B. Roberts, Phys. Rev. A **86**, 062512 (2012).
[23] C. S. Wood, S. C. Bennett, D. Cho, B. P. Masterson, J. L. Roberts, C. E. Tanner, and C. E. Wieman, Science **275**, 1759 (1997).
[24] S. C. Bennett and C. E. Wieman, Phys. Rev. Lett. **82**, 2484 (1999).
[25] J. Guena, D. Chauvat, P. Jacquier, E. Jahier, M. Lintz, S. Sanguinetti, A. Wasan, M. A. Bouchiat, A. V. Papoyan, and D. Sarkisyan, Phys. Rev. Lett. **90**, 143001 (2003).
[26] C. S. Wood, S. C. Bennett, J. L. Roberts, D. Cho, and C. E. Wieman, Can. J. Phys. **77**, 7 (1999).
[27] J. R. Persson, At. Data Nucl. Data Tables **99**, 62 (2013).
[28] J. R. Persson, At. Data Nucl. Data Tables **154**, 101589 (2023).
[29] A. P. Galvan, Y. Zhao, L. A. Orozco, E. Gomez, A. D. Lange, F. Baumer, and G. D. Sprouse, Phys. Lett. B **655**, 114 (2007).
[30] G. Sanamyan, B. M. Roberts, and J. S. M. Ginges, Phys. Rev. Lett. **130**, 053001 (2023).
[31] G. Grynberg and B. Cagnac, Rep. Prog. Phys. **40**, 791 (1977).
[32] K. D. Bonin and T. J. McIlrath, J. Opt. Soc. Am. B **1**, 52 (1984).
[33] M. Goppert-Mayer, Ann. Phys. **18**, 466 (2009).
[34] L. S. Vasilienko, V. P. Chebotaev, and A. V. Shishaev, JETP Lett. **12**, 113 (1970).
[35] A. Corney, *Atomic and Laser Spectroscopy* (Clarendon Press, Oxford, 1977), Chap. 18.
[36] E. Fermi and E. Segre, Z. Phys. **82**, 729 (1933).
[37] A. Bohr and V. F. Weisskopf, Phys. Rev. **77**, 94 (1950).
[38] H. J. Rosenberg and H. H. Stroke, Phys. Rev. A **5**, 1992 (1972).
[39] D. A. Steck, Rubidium 85 D Line Data, https://steck.us/alkalidata/rubidium85numbers.pdf (revision 2.3.3, 28 May 2024).
[40] D. A. Steck, Rubidium 87 D Line Data, https://steck.us/alkalidata/rubidium87numbers.pdf (revision 2.3.3, 28 May 2024).
[41] F. Biraben, M. Bassini, and R. Cagnac, J. Phys. France **40**, 445 (1979).
[42] J. Marek and P. Munster, J. Phys. B **13**, 1731 (1980).
[43] N. D. Zameroski, G. D. Hager, C. J. Erickson, and J. H. Burke, J. Phys. B **47**, 225205 (2014).
[44] A. A. Buchheit and G. Morigi, Phys. Rev. A **94**, 042111 (2016).
[45] B. Rahaman, S. C. Wright, and S. Dutta, Phys. Rev. A **109**, 042820 (2024).
[46] A. Perez Galvan, Y. Zhao, and L. A. Orozco, Phys. Rev. A **78**, 012502 (2008).
[47] R. Gupta, W. Happer, L. K. Lam, and S. Svanberg, Phys. Rev. A **8**, 2792 (1973).
[48] M. S. Safranova, W. R. Johnson, and A. Derevianko, Phys. Rev. A **60**, 4476 (1999).
[49] C. W. White, W. M. Hughes, G. S. Hayne, and H. G. Robinson, Phys. Rev. **174**, 23 (1968).
[50] H. T. Duong, C. Ekstrom, M. Gustafsson, T. T. Inamura, P. Juncar, P. Lievens, C. Lindgren, S. Matsuki, T. Murayama, R. Neugart, T. Nilsson, T. Nomura, M. Pellarin, J. P. S. Penselin, J. Pinard, I. Ragnarsson, O. Redi, H. H. Stroke, J. L. Vialle, and the ISOLDE Collaboration, Nucl. Instrum. Methods Phys. Res., Sect. A **325**, 465 (1993).
[51] E. Arimondo, M. Inguscio, and P. Violino, Rev. Mod. Phys. **49**, 31 (1977).
[52] I. Barmes, S. Witte, and K. S. E. Eikema, Phys. Rev. Lett. **111**, 023007 (2013).
[53] J. S. M. Ginges and V. V. Flambaum, Phys. Rep. **397**, 63 (2004).
[54] E. Gomez, L. A. Orozco, and G. D. Sprouse, Rep. Prog. Phys. **69**, 79 (2006).